LANGMUIR

pubs.acs.org/Langmuir Article

Nonequilibrium Self-Organization of Lipids into Hierarchically Ordered and Compositionally Graded Cylindrical Smectics

James C. S. Ho, Wan-Chih Su, Xuan Chun Wang, Atul N. Parikh,* and Bo Liedberg*

Cite This: *Langmuir* 2022, 38, 1045−1056 Read Online

ACCESS | Metrics & More | Article Recommendations | Supporting Information

Downloaded via UNIV OF CALIFORNIA DAVIS on May 30, 2022 at 17:37:09 (UTC).
See https://pubs.acs.org/sharingguidelines for options on how to legitimately share published articles.

ABSTRACT: When a dry mass of certain amphiphiles encounters water, a spectacular interfacial instability ensues: It gives rise to the formation of ensembles of fingerlike tubular protrusions called myelin figures—tens of micrometers wide and tens to hundreds of micrometers long—representing a novel class of nonequilibrium higher-order self-organization. Here, we report that when phase-separating mixtures of unsaturated lipid, cholesterol, and sphingomyelin are hydrated, the resulting myelins break symmetry and couple their compositional degrees of freedom with the extended myelinic morphology: They produce complementary, interlamellar radial gradients of concentrations of cholesterol (and sphingomyelin) and unsaturated lipid, which stands in stark contrast to interlamellar, lateral phase separation in equilibrated morphologies. Furthermore, the corresponding gradients of molecule-specific chemistries (i.e., cholesterol extraction by methyl-β-cyclodextrin and GM_1 binding by cholera toxin) produce unusual morphologies comprising compositionally graded vesicles and buckled tubes. We propose that kinetic differences in the information processing of hydration characteristics of individual molecules while expending energy dictate this novel behavior of lipid mixtures undergoing hydration.

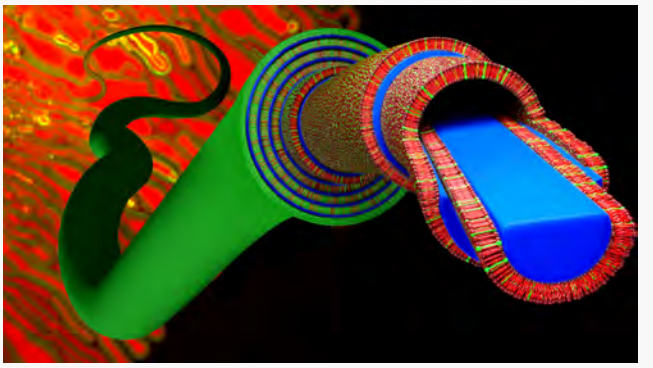

INTRODUCTION

Aqueous phase self-assembly of amphiphilic molecules, such as surfactants, lipids, and block copolymers, at thermodynamic equilibrium is now substantially well understood.[1,2] But the kinetic pathways, which unfold when an almost insoluble phase of lamellar surfactant meets water, remain incompletely understood. During this intrinsically nonequilibrium, energy-dissipating process, the hydrating amphiphile organizes supramolecularly and relaxes dynamically, traversing down a complex free-energy landscape dotted with multiple local minima and metastable intermediates. Depending on the details of the initial conditions, it can give rise to novel instabilities, generate spatial and temporal patterns, and produce kinetically trapped metastable states *en route* to thermal equilibrium.[3−5]

Depending on the energetics of the system, two distinct scenarios emerge: (1) kinetic assemblies, where the hydrating amphiphilic assembly becomes trapped in a local minimum of the free-energy landscape, and (2) far-from-equilibrium, active assemblies, which persist as long as the energy supply lasts.[6] In both cases, the resulting supramolecular organization propagates amphiphilic self-assembly over extended and multiple length scales. Moreover, the facile transitions between multiple local free-energy minima, separated by accessible activation energy barriers, render the organization dynamic, sensitive to subtle perturbations from the environment. Consequently, both kinetic and far-from-equilibrium supramolecular systems consisting of even single amphiphiles can access higher-order organizational states producing complex and dynamic morphologies[4,6]—far surpassing the ordering and behaviors of supramolecular assemblies achievable under equilibrium conditions.

Perhaps, one of the most striking examples of such higher-order self-assembly of amphiphiles under nonequilibrium conditions is the class of transient, but long-lived, structures, called myelin figures (myelins). First reported by Virchow more than 150 years ago,[7,8] myelins appear during the dissolution of many common surfactants and lipids. They emerge at the lipid-water boundary as large ensembles of fingerlike tubular protrusions—tens of micrometers wide and tens to hundreds of micrometers long—when a dry mass of certain fluid-phase lipids encounters water. Individual myelin grows sinuously by a two-dimensional reptation-like motion, which tightly juxtaposes with their neighbors, cooperatively elongates, and often folds into symmetry-breaking helical shapes.

Received: September 27, 2021
Revised: December 30, 2021
Published: January 12, 2022

ACS Publications © 2022 American Chemical Society

A considerable body of experimental and theoretical effort has sought to identify mechanisms underlying their formation,[9−14] characterize their growth mechanisms,[9−20] deduce their structural organization,[14,21−24] and delineate their higher-order dynamics including coiling.[11,25,26] The cumulated weight of these studies suggests that myelins represent a kinetic intermediate between the lamellar phase and the phase characterized by dispersion of multilamellar vesicles. Despite their superficial resemblance, they do not represent a true classical diffusive fingering instability (Mullins−Sekerka instability) in which growth proceeds by preferential accumulation at the exposed tip.[27] Instead, experimental evidence supports a picture in which myelins grow from their roots at the boundary between the aqueous phase and the lipid reservoir.[10] Although precise microscopic description of their formation mechanism continues to be debated, it is clear that they form in response to the hydration gradient (or osmotic stress) between the amphiphilic phase and pure water.[10,14]

Structurally, myelin figures represent an unusual class of lyotropic smectic liquid crystal. They are organized into discrete tubules consisting of thousands of cylindrically stacked alternating lamellae of lipid bilayers and aqueous channels wrapping a central (∼100 nm) aqueous core.[22−24]The fluid character of the surfactants facilitates in-plane two-dimensional (2D) lateral diffusion of individual lipids within each cylindrical lamellae. Within the cylindrical stacks of myelin figures, the thermally excited out-of-plane undulation fluctuations are expected to be suppressed by the spatial confinement due to neighboring layers. The corresponding entropy loss gives rise to the interlamellar repulsive interactions—the so-called Helfrich repulsion—which stabilizes the one-dimensional smectic order in myelins[28] and inhibits molecular exchanges between individual lamellae. Taken together, the myelinic organization exemplifies a class of discrete supramolecular structures displaying multiple levels of ordering including primary self-assembly of amphiphilic molecules into bilayers; secondary reorganization of these discrete bilayers into a smectically ordered cylindrical lamellar phase; and occasional tertiary organization of single myelin figures into symmetry-breaking helices, braids, and coils.

The elaborate ordering and dynamics of myelin figures above, prompted by their nonequilibrium hierarchical information processing,[29] raises an intriguing question: How would mixtures of amphiphiles organize within such dynamic myelin instabilities? Equilibrium phase diagrams of many bilayer-forming amphiphilic (e.g., lipidic) mixtures display rich phase behaviors. Even the simplest binary and ternary mixtures of fluid-phase lipids—with only subtle differences in their molecular make-ups and preferential interactions—phase-separate into coexisting fluid phases stabilizing spatial heterogeneities in single lipid bilayers at equilibrium.[30−32] This in turn prompts additional questions: (i) Would equilibrium phase separation of lipids in single bilayers be reproduced in individual lamellae of myelins? (ii) If yes, would in-plane compositional degrees of freedom induce higher-order interlayer organization of domains within the cylindrical smectic phase of myelins? (iii) If not, what factors will determine the spatial organization of lipids within myelins? (iv) How would the initial interfacial instability, which propels myelin growth, be modified by the presence of phase-separating mixtures of lipids. Motivated by these questions, we experimentally investigate here the formation of myelin figures using a multicomponent lipid mixture as a source.

In this study, we study myelin figures produced from mixtures of phase-separating lipids using fluorescence microscopy. Our results reveal a surprising gradient organization characterizing lipid distribution across different myelin lamellae. In stark contrast to intralamellar phase separation in equilibrated structures, we find that the molecules comprising individual myelins segregate differentially across different lamellae producing a radial and continuous concentration gradient of the order parameter, i.e., molecular concentration: cholesterol (and sphingomyelin) concentrations are the highest in the outer lamellae with continuously decaying concentrations inward culminating with an essentially cholesterol (and sphingomyelin)-depleted phospholipid phase in the innermost lamellae. A natural consequence of this concentration distribution then is the emergence of corresponding radial gradients of physical−chemical properties, including lateral fluidity, bending rigidity, water permeability, and chemical reactivity—all within the single, consolidated smectic phase.[33] Based on observations of dynamic repartitioning of lipid amphiphiles at the interface, we propose that this emergent, higher-order spatiotemporal self-organization is driven not by any preexisting phase separation of the lipids in the dry mass. But rather the differences in the kinetic information processing of different molecular components during hydration dictate this transient, but long-lived, response of lipid mixtures.

MATERIALS AND METHODS

Materials. 1-Palmitoyl-2-oleoyl-*sn-glycero*-3-phosphocholine (POPC), 1,2-dipalmitoyl-*sn-glycero*-3-phosphoethanolamine-*N*-(lissamine rhodamine B sulfonyl) (Rhod-PE), 1,2-dioleoyl-*sn-glycero*-3-phosphoethanolamine-*N*-(7-nitro-2-1,3-benzoxadiazol-4-yl) (NBD-PE), egg sphingomyelin (sphingomyelin), cholesterol, and ganglioside GM_1 were purchased from Avanti Polar Lipids (Alabaster, Alabama). Methyl-β-cyclodextrin (MβCD), 6-dodecanoyl-*N*,*N*-dimethyl-2-naphthylamine (Laurdan), and 6-propionyl-2-(dimethylamino)-naphthalene (Prodan) were purchased from Sigma-Aldrich (Singapore). Alexa Fluor 488-conjugated cholera toxin subunit b (AF488-CTxB) was purchased from Thermo Fisher Scientific (Waltham, MA).

Formation of Myelin Figures. We used a well-studied system of ternary lipid mixture consisting of 1-palmitoyl-2-oleoyl-*sn-glycero*-3-phosphocholine (POPC), cholesterol, and sphingomyelin. Equilibrium phase diagram of this mixture predicts microscopic phase separation characterized by two coexisting liquid phases: a dense phase enriched in sphingomyelin and cholesterol designated as the L_o (liquid-ordered) phase and a second, less dense L_d (liquid-disordered) phase consisting primarily of POPC.[34] For comparions, we also prepared single-component myelin figures using POPC.

Stock solutions of lipid in chloroform were first prepared: POPC (25 mg mL^{-1}), POPC/Rhod-PE (99.9:0.1, mol %, 25 mg mL^{-1}), POPC/sphingomyelin/cholesterol (33:33:33, 30:50:20 or 45:45:10, mol %, 12.5 mg mL^{-1}), POPC/sphingomyelin/cholesterol (33:33:33, 30:50:20 or 45:45:10, mol %, 12.5 mg mL^{-1}) doped with 0.1 mol % Rhod-PE and/or 0.1 mol % NBD-PE, and POPC/sphingomyelin/cholesterol/GM_1 (33:33:33, 30:50:20, or 45:45:10, mol %, 12.5 mg mL^{-1}) doped with 0.1 mol % Rhod-PE.

Our typical experimental configuration (Figure S1), which we adapted from previous studies,[12,14,17] was as follows. A small drop (≤8 μL, total of 100 μg of lipid) of a lipid stock solution was dropped (e.g., for 8 μL of solution, 2 × 4 μL) onto a microscopy glass cover slide, which was freshly cleaned with chloroform. The organic solvent was allowed to evaporate for at least 15 min under house vacuum. Subsequently, a second glass cover slide was gently pressed onto the

https://doi.org/10.1021/acs.langmuir.1c02576
Langmuir 2022, 38, 1045−1056

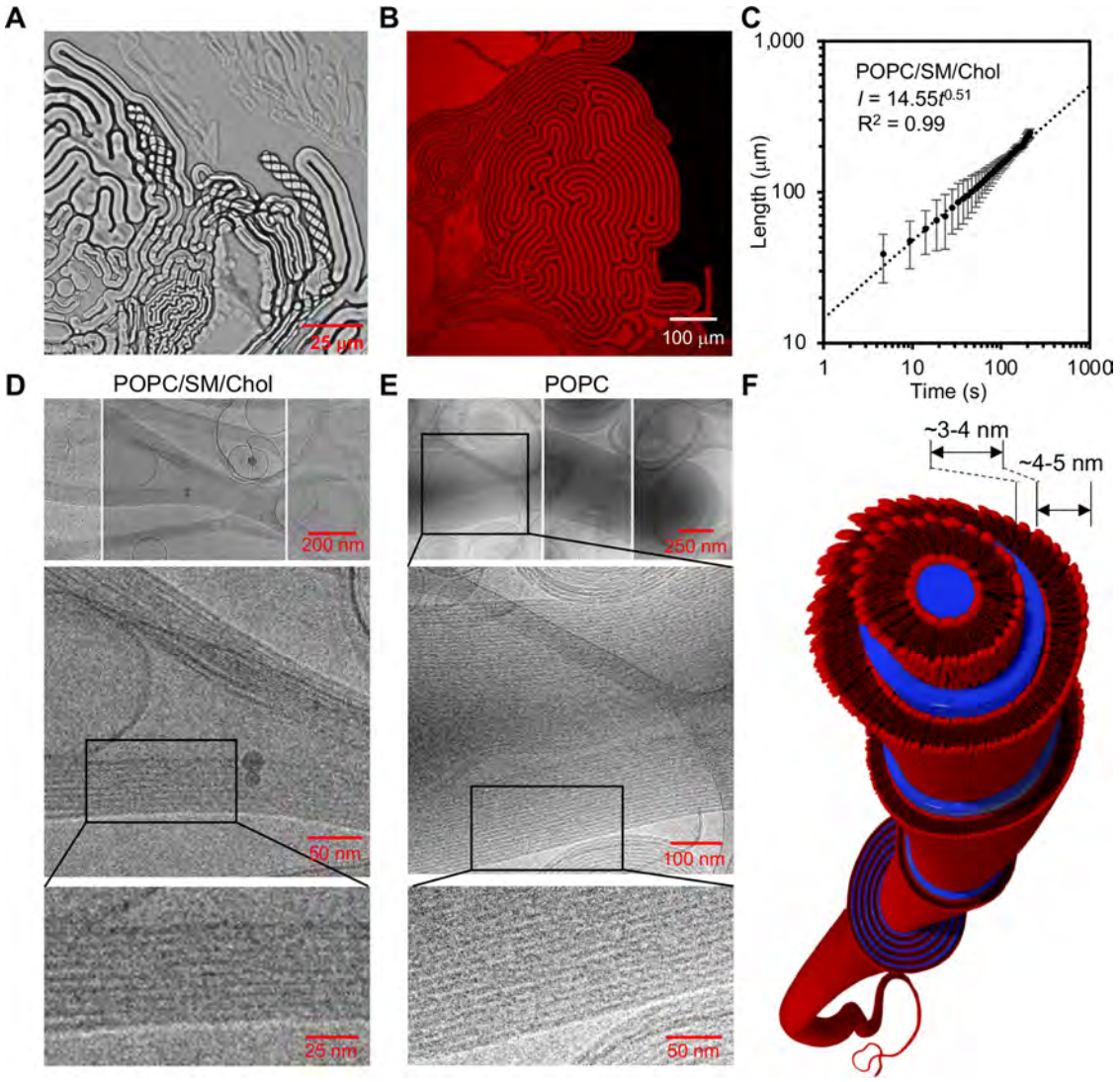

Figure 1. Structural characterization of myelin figures. (A) Optical micrograph and (B) fluorescence micrograph of POPC myelin figures, grown for about 90 mins. (C) Time dependence of average myelin length (n = 4). Error bars refer to S.D. The dotted line is the power law fit. (D, E) Cryogenic transmission electron micrographs of (D) POPC/sphingomyelin (SM)/cholesterol (Chol) (33:33:33 mol %) and (E) POPC myelin figures. The top panels are manual stitching of multiple images to depict the elongated protrusions. (F) Cartoon depicting single-component POPC myelin figure. The blue region represents the aqueous interlamellar space. Geometrical details are shown. Note: the central aqueous core is not drawn to scale.[22−24]

lipid cake to create a well-defined lipid−air boundary (sandwich configuration). Deionized water or solute-laden aqueous phases (40 μL) were then allowed to infuse into the sandwich via capillarity, and the ensuing changes were monitored in real time using optical and fluorescence microscopies (Figure S1).

Alternate experimental configurations employing dry lipid on a single glass cover slide or lipid-laden interior surfaces of capillaries[35] were used to prepare myelins for characterization by cryo-transmission electron microscopy (cryo-TEM) and small-angle X-ray scattering (SAXS), respectively. The fact that these alternate sample preparation methods reproducibly produce myelin figures has been previously established.[17] For characterization by cryo-transmission electron microscopy (cryo-TEM), deionized water (40 μL) was added directly to the dry lipid cake. Myelin figures were allowed to grow for 30−60 min. The myelin-containing solution (4 μL) was aspirated gently for cryo-TEM grid preparation. For small-angle X-ray scattering (SAXS) experiment, a small drop (≲8 μL, total of 100 μg of lipid) of a lipid stock solution was added in succession (e.g., for 8 μL of solution, 2 × 4 μL) into a borosilicate capillary tube (1 mm diameter and 0.01 mm wall thickness) and allowed for the removal of chloroform under house vacuum. Deionized water (∼10 μL) was added into the capillary tube, and the tube was immediately sealed. Myelin figures were allowed to grow for 30−60 min before measurement.

Growth Analysis of Myelins. Dry lipid cakes prepared in the sandwich configuration were used for growth analysis. The length of individual myelin was measurement using a segmented line tracing the central core of the myelin. All measurements were performed using public-domain Fiji ImageJ software.

Optical and Fluorescence Microscopy and Image Analysis. Wide-field fluorescence microscopy images were acquired using a DeltaVision microscope (Applied Precision, Inc., Issaquah, WA) fitted with 10×/0.40 and 20×/0.75 objectives (Olympus, Tokyo, Japan), 4′,6-diamidino-2-phenylindole (DAPI), tetramethylrhodamine isothiocyanate (TRITC) and fluorescein isothiocyanate (FITC) Semrock filters (New York, NY), and a mercury lamp (Intensilight C-HGFIE, Nikon Corporation, Tokyo, Japan). Images were processed using Softworx 4.1.0 (Applied Precision, Inc., Issaquah, WA) or ImageJ. Confocal microscopy images were acquired on an inverted Nikon Eclipse TE 2000 microscope (Nikon Corporation, Tokyo, Japan) fitted with an X-Light spinning disk confocal unit (CrestOptics, Rome, Italy) and an Andor iXon+ EMCCD camera

https://doi.org/10.1021/acs.langmuir.1c02576
Langmuir 2022, 38, 1045−1056

(Andor Technology, Belfast, Northern Ireland). Additional image analysis was performed in Fiji ImageJ.

Cryogenic Transmission Electron Microscopy (Cryo-TEM). For characterization by cryo- TEM, a dry lipid cake was prepared as described above. Electron microscope grids, coated with a lacey holey carbon-coated Cu grid, 200 mesh (Quantifoil, Großlöbichau, Germany) were glow-discharged for 20 s and used immediately. A solution (4 μL) containing preformed myelins was deposited onto a grid at 99% humidity, blotted (blot time of 1 s, blot force of 1) with Whatman filter paper (GE Healthcare Bio-Sciences, Piscataway, NJ), and plunged into liquid ethane (Vitrobot, FEI Europe B.V., Eindhoven, the Netherlands). The cryo-grids were imaged using a FEG 200 keV transmission electron microscope (Arctica, FEI Europe B.V., Eindhoven, the Netherlands) equipped with a direct electron detector (Falcon II, Fei Europe B.V., Eindhoven, the Netherlands). Line scans to plot density distribution across high- and low-density features were carried out in Fiji ImageJ.

Small-Angle X-ray Scattering (SAXS). For small-angle X-ray scattering (SAXS) experiment, myelins were prepared in a borosilicate capillary tube as described above and measured within 30−60 min after hydration. All measurements were performed using a Nanoinxider instrument (Xenocs SAS, Grenoble, France) in transmission mode, and silver behenate was used for calibration. The lamellar repeat distance d (lipid bilayer with an adjacent water layer) was calculated using the equation $d = 2n\pi/(q)$, with n being the order number of the diffraction peak and q is the scattering vector, defined by the equation $q = (4\pi/\lambda)\sin\theta$, where λ is the wavelength (1.5419 Å) and θ is the scattering angle. Data analysis was performed using FOXTROT application (Xenocs).

Fluorescence Recovery after Photobleaching (FRAP). FRAP experiments were performed on a fluorescence microscope equipped with spinning disk confocal configuration using an Intelligent Imaging Innovations Marianas Digital Microscopy Workstation (3i Denver, CO) fitted with a CSU-X1 spinning disk head (Yokogawa Musashino, Tokyo, Japan), a QuantEM512SC EMCCD camera (Photometrics Tuscon, AZ), and an oil immersion 63× objective (Zeiss Plan-Fluor 63× (NA 1.4), Carl Zeiss Oberkochen, Germany). Rho-B DOPE and NBD-PE fluorescent probes were bleached in a circular region (∼2 to 3 μm in radius) at 100% of maximal laser power. Recovery of fluorescence was recorded and measured from the subsequent frames, 10 frames per second.

Generalized Polarization (GP) Image Analysis. Stock solutions of 1 mM Laurdan and 100 μM Prodan were prepared in methanol and ethanol, respectively, and either used fresh or stored at −20 °C. Laurdan or Prodan was added to the lipid stock solution at 1 mol % for subsequent dry lipid cake preparation, according to the sandwich configuration procedures described above. Two-channel images were acquired using two designated filter sets (DAPI/DAPI and DAPI/FITC) with identical exposure setting. GP analysis of the images was performed in Fiji ImageJ based on the following format

$$\mathrm{GP} = \frac{\mathrm{Image}_{\mathrm{DAPI/DAPI}} - \mathrm{Image}_{\mathrm{DAPI/FITC}}}{\mathrm{Image}_{\mathrm{DAPI/DAPI}} + \mathrm{Image}_{\mathrm{DAPI/FITC}}}$$

where $\mathrm{Image}_{\mathrm{DAPI/DAPI}}$ and $\mathrm{Image}_{\mathrm{DAPI/FITC}}$ refer to image acquired using DAPI/DAPI and DAPI/FITC filter sets, respectively, following the classical equation

$$\mathrm{GP} = \frac{I_{440} - I_{490}}{I_{440} + I_{490}}$$

where I_{440} and I_{490} refer to the steady-state fluorescence emission intensities at 440 and 490 nm, respectively.

Methyl β-Cyclodextrin (MβCD) and Cholera Toxin Subunit b (CTxB) Treatments. For the morphological characterization of MβCD or CTxB treatment, a dry lipid cake consisting of POPC/sphingomyelin/cholesterol (33:33:33, mol %) was prepared as described above. For MβCD treatment, the lipid stock solution was doped with 0.1 mol % Rhod-PE and 0.1 mol % NBD-PE. For CTxB treatment, the lipid stock solution was doped with 0.1 mol % Rhod-PE. Deionized water (40 μL) was added directly onto the dry lipid cake. Myelin figures were allowed to grow for about 30 min. Subsequently, MβCD (2−5 μM) or AF488-CTxB (0.25−1 mM) was added to the hydration solution and the additive was let to diffuse to the myelins to initiate morphological transitions. Wide-field fluorescence microscopy images were acquired on a DeltaVision microscope with FITC and TRITC filters sets.

RESULTS AND DISCUSSION

Hydration-Induced Formation of Multicomponent Myelins. We begin by probing the hydration of lipid plaques. We compare mixed-composition plaques consisting of a ternary mixture of equimolar concentrations of POPC, cholesterol, and sphingomyelin with plaques composed of single, fluid-phase lipid, namely, POPC. Monitoring the hydration-induced changes at the lipid−water boundary in real time using optical microscopy confirm, for both cases, the formation of a dense tangle of tubes emanating from the incipient lipid−water boundary (Videos S1 and S2). The tubes grow sinuously, juxtapose tightly, and occasionally coil into chiral symmetry-breaking helices (Figure 1A). The overall morphologies they produce are strikingly reminiscent of labyrinthine patterns of typical reaction-diffusion systems[36] (Figure 1B). Quantifying the growth behavior of multicomponent myelins confirms the expected square root of time dependence (Figure 1C), reported previously for densely packed myelins.[10,14,18]

To confirm that the multilamellar nature of the myelins is also preserved for the multicomponent myelin figures, we used a combination of cryo-TEM and SAXS measurements (Figures 1D−E and S2A,B). A representative cryo-TEM image for the ternary myelins is characterized by a pattern of alternating light and dark bands surrounding a larger central core with individual bands remaining parallel, distinctly separated from their neighbors and merging only at the single bulging free ends (Figure 1D). These features already confirm the tubular motif, linear nature, and the essential coaxial multilamellarity (rather than cochleate-like scroll structure[37]) of myelins. Electron scattering profiles across multiple dark and light bands for multicomponent myelins yield average thicknesses of 5.9 ± 1.0 nm (n = 38, where n refers to the number of bands measured) and 2.7 ± 0.5 nm (n = 36), respectively. The former is consistent with the thickness of a single phospholipid bilayer, and the latter is comparable to the width of the interbilayer space.[38] The independent assessment of a single repeating unit, combining a pair of light and dark bands, averages at 8.3 ± 1.1 nm (n = 10, where n refers to the band periodicity for the light−dark pair), characterizing the smectic pattern.[22−24] The overall structure of the ternary myelin is generally comparable to that of POPC myelins, characterized by 4.4 ± 0.6 nm (n = 21) and 3.7 ± 0.5 nm (n = 21) for the lipid bilayer and interbilayer spacings, respectively (Figure 1E). This essential organization of the ternary component myelins is further supported by preliminary SAXS measurements (Figure S2A,B).

Collectively, our preliminary comparison confirms that the multicomponent myelins qualitatively reproduce all major structural and dynamical properties of single-component myelins (Figure 1F). They confirm previous findings that the molecular organization of myelin figures resembles that of a lyotropic smectic liquid crystal in cylindrical geometry:[22−24] concentric arrays of discrete tubules consisting of thousands of cylindrically stacked alternating lamellae of lipid bilayers and aqueous channels wrapping a central (ca. 100−200 nm)

https://doi.org/10.1021/acs.langmuir.1c02576
Langmuir 2022, 38, 1045−1056

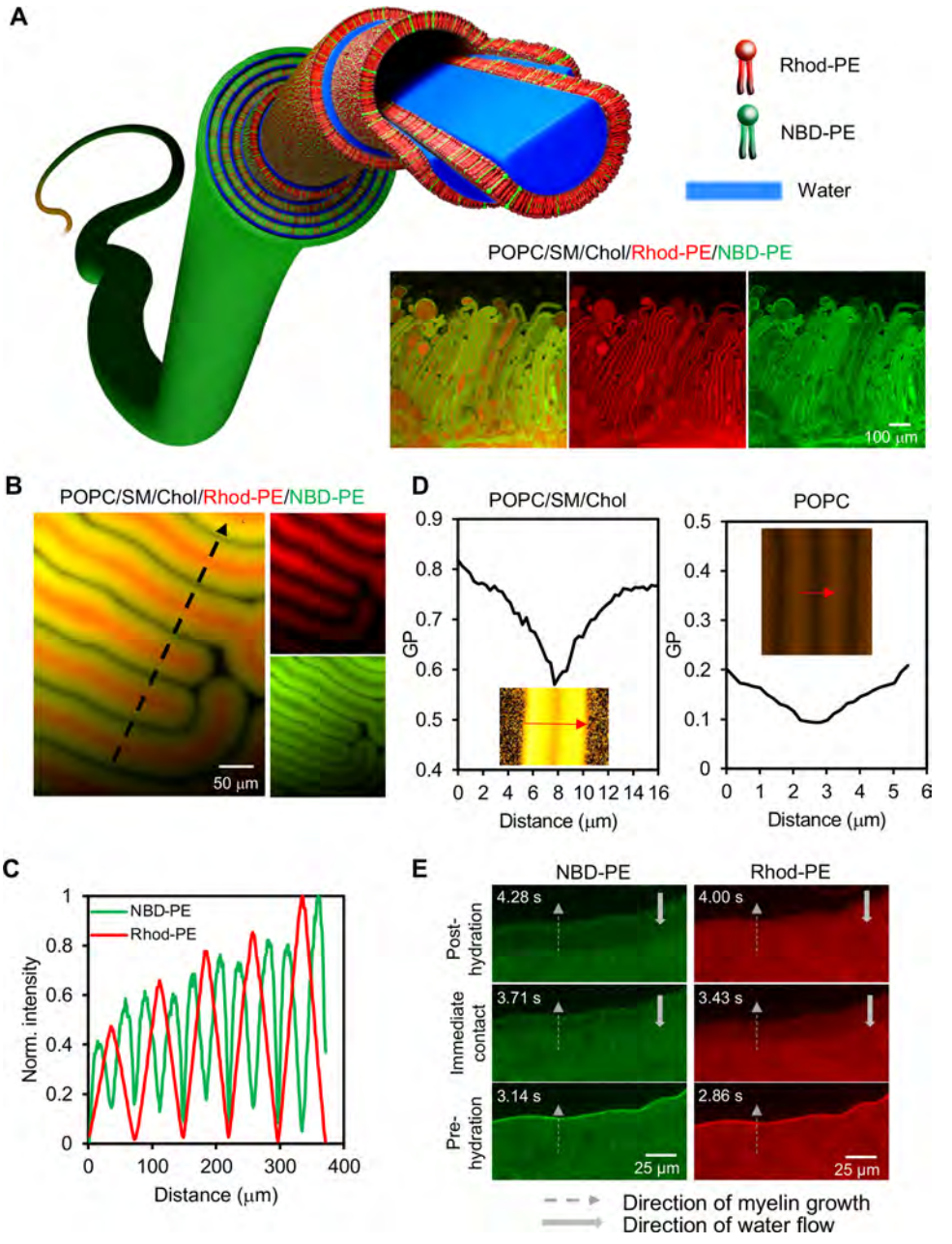

Figure 2. Compositionally graded myelin figures. (A) Cartoon depicting a compositionally graded myelin figure. Red and green structures represent Rhod-PE and NBD-PE, respectively. The blue region represents the aqueous interlamellar space. The central aqueous core is not drawn to scale.[22−24] Fluorescence micrographs at the bottom right panel show typical POPC/sphingomyelin (SM)/cholesterol (Chol) (33:33:33 mol %) myelin figures, doped with 0.1 mol % of Rhod-PE and 0.1 mol % NBD-PE, grown for about 30 min, in merged and split channels. (B) Confocal fluorescence micrograph of POPC/SM/Chol/Rhod-PE/NBD-PE myelin figures. (C) Line intensity profiles of Rhod-PE and NBD-PE in (B). The black dashed line in (B) shows the measured region. (D) Laurdan generalized polarization (GP) analysis of POPC/SM/Chol and POPC myelin figures. The red arrows in the insets show the measurement region. (E) Fluorescence micrographs show the distribution of Rhod-PE and NBD-PE fluorophores at the instance of water−lipid contact (middle), pre- (bottom), and post- (top) hydration states.

aqueous core.[22−24] Further characterization of the distribution of molecular components within these multicomponent myelins, however, reveals a striking new feature, presented below.

Emergence of Radial Compositional Gradients in Multicomponent Myelin Figures. When the multicomponent myelins were visualized by doping the initial lipid mixture with two phase-sensitive fluorescent dye-conjugated lipids (ca. 0.1−0.5 mol %),[39−43] individual myelins displayed the remarkable appearance of complementary gradients in fluorescence emission characteristics: The emission due to NBD-PE (green) was the highest in the outer lamellae and that due to Rhodamine-PE (Rhod-PE, red) was the highest in the innermost lamellae in the vicinity of the core (Figure 2A). The intensities of both fluorophores displayed continuous radial gradients, with the green decaying outside-in and the red decaying inside-out (Figure 2B,C). Because the two fluorophore-conjugated lipids have phase- and composition-sensitive partitioning characteristics, the observed gradients in emission intensities can be readily interpreted to indicate the

https://doi.org/10.1021/acs.langmuir.1c02576
Langmuir 2022, 38, 1045−1056

existence of continuous compositional gradient across individual lamellae comprising the myelin figures. Specifically, NBD-PE partitions preferentially in denser, cholesterol-enriched L_o phases and Rhod-PE prefers cholesterol-depleted and phospholipid enriched, more fluid L_d phases.[40] Thus, our observations of their complementary and continuous gradients indicate the enrichment of cholesterol and sphingomyelin in the outermost lamellae and conversely that of phospholipid POPC in the innermost lamellae with each decaying in radially opposite directions.

It is also notable that the fluorescence intensities do not exhibit any measurable intensity variations along the main axis of the myelin figures at fixed radii. In other words, we find no evidence for intralamellar phase separation. This is not surprising for the outer- and innermost lamellae, which contain limiting concentrations of the L_o and L_d phase components, both of which can be expected to produce single uniform phases.[34] But the existence of continuous gradients of molecular compositions in single myelins suggests that the compositions of individual lamellae within single myelins must span a broad region of the phase diagram, including the coexistence region. This gradient organization is fully reproducible over several different compositions. For three different compositions, 30:50:20, 33:33:33, and 40:10:50, each of which resides in the phase coexistence region of the miscibility phase diagram,[34] we find fully reproducible radial patterns of molecular compositions (Figure S3).

This appearance of radial compositional gradients in multicomponent myelins stands in stark contrast to previous observations of molecular organization in planar multilayer stacks of lipid bilayers. Previous studies characterizing molecular organization in planar multilamellar membranes reveal in-plane phase separation of cholesterol and sphingomyelin-rich liquid-ordered phase from the fluid-phase POPC and the appearance of long-range interlamellar stacking of intralamellar domains—consistent with the formation of an equilibrated smectic phase.[44,45] This then raises the possibility that the molecular organization in myelin figures might not be at equilibrium.

The question of equilibration of myelin figures has been of a long-standing debate. One school suggests that once formed by an initial instability, myelin figures achieve a fully swollen lamellar organization. Thus, this line of reasoning argues that they must be in local equilibrium with the surrounding aqueous phase.[10,14,18] An alternate model proposes that the myelin figures are dynamic structures, produced by an elastic instability, which requires a sustained driving force—a continuous consumption of the osmotic energy due to the water chemical potential gradient at the lipid−water boundary of the hydrating lipid mass.[12] In our case, since intralayer phase separation and thus interlamellar stacking are both suppressed (instead producing interlamellar compositional gradient), these support the picture that myelins represent a class of stress-generated, driven instabilities.[12] Thus, our observations of sustained compositional gradients, even after extended periods of time (tens of minutes to hours), lend further credence to the notion that the structure is not locally equilibrated.

Why doesn't cholesterol equilibrate between the myelin lamellae? Although isolated cholesterol molecules have limited solubility in bulk water, the interlamellar aqueous phase is small and the surface area is large. As a result, it seems plausible that cholesterol may equilibrate between layers. We reason that the strong association of cholesterol with sphingomyelin—which is the basis for the formation of liquid-ordered phases—limits cholesterol equilibration between myelin lamellae, thereby stabilizing cholesterol gradient such as observed. But this proposition remains unverified.

The appearance of sustained interlamellar gradients of composition, with each lamella differing in composition from its neighbors, should give rise to corresponding gradients of molecular packing and thus of lateral fluidity between individual lipid bilayers comprising the consolidated smectic phase. To consider this scenario, we doped the initial lipid plaque with Laurdan, an environment-sensitive fluorescent probe, whose emission characteristics report on the local state of hydration at the lipid headgroup−acyl chain interfacial region: In general, partitioning of Laurdan within a more ordered lipid phase produce higher generalized polarization (GP) value and vice versa.[46] The GP values for the myelins derived from the Laurdan-doped lipid mass clearly reveal a continuous gradient: The lowest GP values were obtained for the innermost lamellae (0.5 ± 0.08, $n = 3$), and conversely, the outermost lamellae yielded the highest values (0.8 ± 0.05, $n = 3$, Figures 2D and S4A). By comparison, POPC myelins, which do not present any compositional gradient, show significantly smaller differences in the GP values across the lamellae (0.1 ± 0.01 to 0.2 ± 0.01, $n = 3$, Figures 2D and S4B). Substituting Laurdan with Prodan, a different but comparable probe, yielded a similar trend in the GP values (data not shown) further confirming the existence of a gradient in chain packing. Additional measurements of lateral fluidity using simple microscopy-based fluorescence recovery after photobleaching experiments confirms the existence of fluidity gradient: When both the L_d phase-partitioning Rhod-PE and the L_o phase-partitioning NBD-PE are photobleached under identical conditions, the former spot is ∼3× broader consistent with the higher fluidity of the probe molecule in the L_d phase (Figure S5).

Taken together, the results presented above reveal how simple hydration of dry lipid mass consisting of phase-separating mixtures of amphiphilic lipids can give rise to an unusual spatiotemporal organization characterized by an extended spatial pattern of chemical composition—a continuous radial gradient of cholesterol (and saturated lipid or sphingomyelin) concentration—within the dynamic myelin-like morphology.

Differential Hydration Kinetics Induces Segregation of Amphiphiles. From a dynamical point of view, the appearance of layer-by-layer gradients of molecular composition in single myelins raises a fundamental question: How do lipids segregate in growing myelins? Since no lipid exchange between individual lamellae of smectically organized myelins can occur, interlamellar segregation of molecules must be determined by the organization in the lamellar phase at the onset of myelinization. Focusing on the early events that characterize myelinic instability, we find a clue. Visualizing the lipid−air interface when water comes into contact with the lipid mass, we find evidence for large-scale molecular sorting (Figures 2E and S6). In the prehydrated state (Figure 2E, bottom images), Rhod-PE and NBD-PE are fully mixed with increased fluorescence at the lipid−air interface. This is consistent with the expected increased concentration of all lipids because of the capillary flow caused by differential evaporation[47] during plaque preparation. The presence of both fluorophore-conjugated lipids at the interface then indicates that the drying process by itself does not segregate lipids at the

https://doi.org/10.1021/acs.langmuir.1c02576
Langmuir 2022, 38, 1045−1056

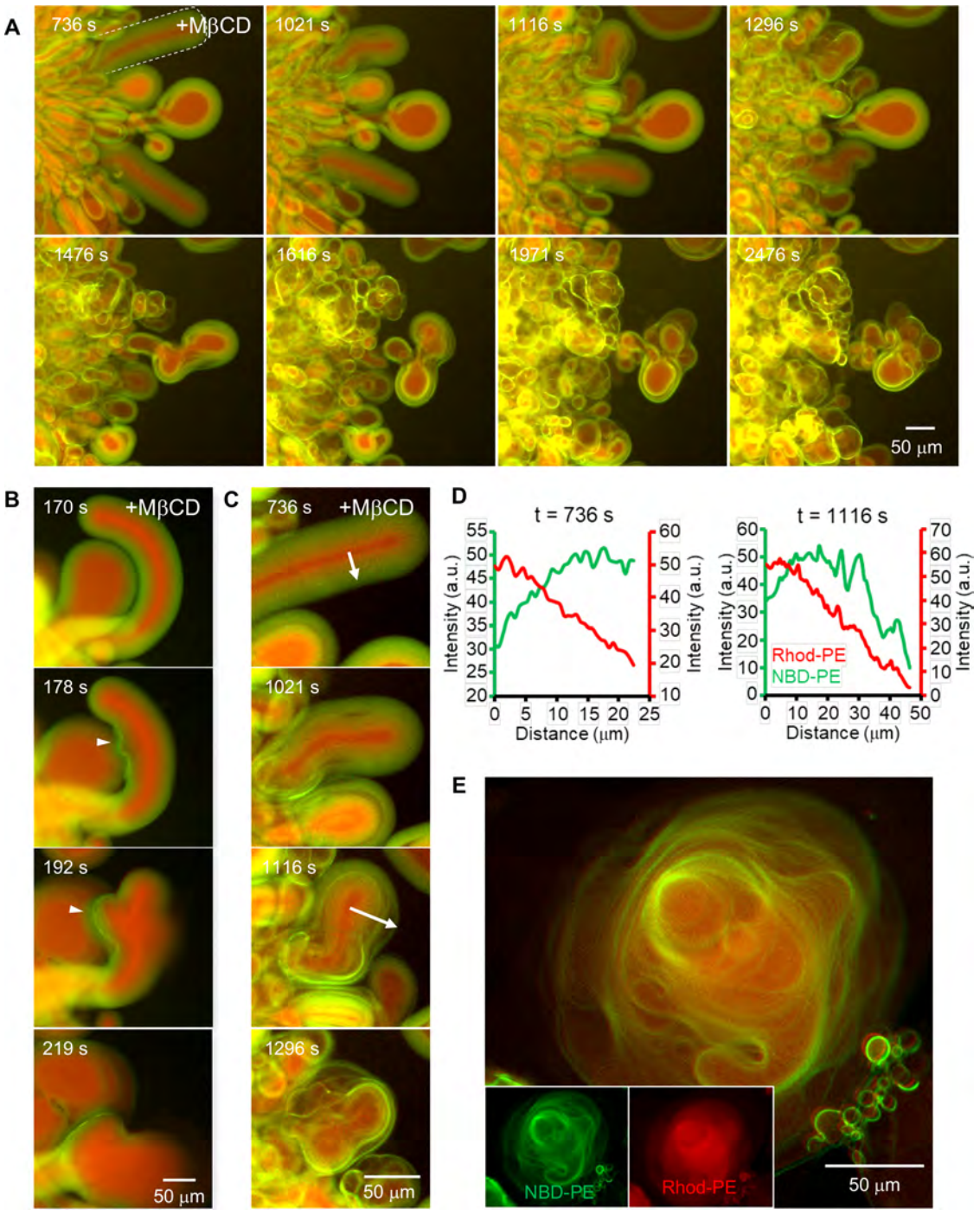

Figure 3. Morphological effects of graded extraction of cholesterol from POPC/SM/Chol/Rhod-PE/NBD-PE myelin figures by methyl *β*-cyclodextrin (M*β*CD). (A) Time-lapse fluorescence micrographs show morphological transition, characterized by a change from tubular to vesicular motif, when myelin figures are subjected to M*β*CD treatment. The morphological evolution and change in lamellar organization of the myelin labeled with a dashed line (t = 736 s) are monitored in (C), and further characterized in (D). (B) Time-lapse fluorescence micrographs highlighting initial deformations of the myelins, characterized by the appearance of multilamellar buds (arrowheads). (C) Time-lapse fluorescence micrographs highlighting the morphological evolution of the myelin marked in (A). (D) Line intensity profiles corresponding to the line arrows indicated in (C) for t = 736 and 1116 s. (E) Compositionally graded multilamellar vesicular structures after M*β*CD treatment.

interface of the dry lipid plaque (Figures 2E, S6, bottom images, and S7, white dotted lines), although some inhomogeneity in lipid distribution is often observed (Figure S7). When water comes into contact with the interface, we find a rapid reorganization at the interface: The enhancement of Rhod-PE intensity is quickly lost, while that of the NBD-PE fluorophore remains (Figures 2E and S6, middle images). Because the two dyes are phase- and composition-sensitive, the observed transient separation of the dyes near the lipid boundary signals incipient phase separation in the lipid plaque just prior to myelin formation. The interfacial depletion of Rhod-PE, which preferentially partitions within the liquid-disordered, POPC-rich phase, then suggests that the amount of POPC at the interface is reduced. Similarly, the unchanged

https://doi.org/10.1021/acs.langmuir.1c02576
Langmuir 2022, 38, 1045−1056

interfacial intensity of NBD-PE, which selectively decorates cholesterol and sphingomyelin-enriched phases suggests that the amount of cholesterol (and sphingomyelin) at the interface remains largely unperturbed. This transient interfacial reorganization in the lipid plaque, prior to myelin formation, can be understood in terms of the known differences in the hydration behaviors of the incipient L_o and L_d phases:[48] Although both cholesterol-rich L_o and POPC-rich L_d phase have comparable hydration-dependent diffusivities, the former experiences much greater activation energy barrier for fluidization.[49,50] It thus seems reasonable that the more mobile L_d phase is selectively transported from the interface by the inward flow of water leaving behind the L_o phase consisting of cholesterol and sphingomyelin to enrich the interface. Within several hundreds of milliseconds, buds of the myelin protrusions are observed (Figure 2E, top images). This initial segregation of molecules, which occurs during the early stage of hydration, characterized by the transformation of the isotropic lipid mass into the lamellar phase, then explains the observed interlamellar molecular segregation in the myelin protrusions. It is also plausible that interlamellar phase separation may serve as a mechanism to lower the elastic bending energy of the L_o phase by reducing the cholesterol content in the inner lamellae.

Molecule-Specific Chemistries Induce Novel Emergent Behaviors and Complex Forms. This interlamellar gradient in cholesterol concentration suggests interesting possibilities for concentration-dependent, molecule-specific chemistries in single myelins (Figure 2A). Constrained by the myelin geometry, these chemistries introduce secondary instabilities, which couple with the initial myelinic instabilities producing novel emergent behaviors and complex forms. In the following, we illustrate these morphological remodeling using two examples: (1) gradient removal of cholesterol using methyl β-cyclodextrin (MβCD) and (2) binding of a L_o phase partitioning ganglioside GM_1 by cholera toxin subunit b (CTxB).

First, the compositional gradients of multicomponent myelins, exhibiting enhanced cholesterol concentrations in the outer lamellae, suggest that the cholesterol content on the outermost lamella may be close to its solubility limit in a lipid bilayer (~66%)[51] decreasing gradually in inner lamellae. As a consequence, the activity of MβCD, a cyclic heptameric oligosaccharide capable of extracting cholesterol from lipid bilayers,[52,53] also can be expected to become radially patterned. To explore the consequences of such spatially graded cholesterol extraction chemistry, we administered MβCD to preformed myelin (POPC/cholesterol/sphingomyelin, 1:1:1 mol/mol ratio, doped with Rhod-PE and NBD-PE). Fluorescence microscopy data indicate a drastic morphological change: The initial tubular motif is abandoned, replaced by rounded, multilamellar structures (Figures 3 and S8−S9 and Videos S3−S5) resembling multilamellar vesicles (MLVs) (Figure 3E). A closer inspection, however, reveals some important differences. While the characteristic smectic arrangement of lamellae of myelin is lost, the concentration gradients are not replaced by uniform compositions across lamellae. A line profile across the lamellae shows that the fluorescence intensity due to Rhod-PE (red) exhibits radial gradient in correspondence with those in the precursor myelins: the highest intensity near the central lumen, decaying toward the periphery of the MLVs (Figures 3D and S9, line profiles). The same however no longer holds for the NBD-PE (green) probe. The initial NBD-PE gradient is now replaced by one exhibiting an uneven distribution, characterized by multiple irregularly spaced peaks in the fluorescence intensity (Figures 3D and S9, line profiles) culminating with the brightest green at the boundary. This in turn suggests that the outer lamellae have a distinctly different composition from the inner ones. Thus, it seems unlikely that the MβCD-mediated cholesterol extraction transforms metastable myelins into equilibrium structures characterized by nested and polydisperse MLVs.[54] Instead, the preservation of the concentration gradient, and thus of the history of MLV formation, suggests a separate nonequilibrium transition.

Remarkably, the observed chemical-stress-mediated transformation of multitubular myelins, upon graded extraction of cholesterol, into multilamellar vesicles bears a striking resemblance to a distinct nonequilibrium transition: shear-induced transformation of the lamellar phase of many common surfactants into a phase consisting of multilamellar vesicles (MLVs), called the "onion" phase.[55,56] There, an application of hydrodynamic sheer has been observed to destabilize the lamellar phase via a cooperative undulatory instability producing MLVs. Moreover, the kinetic process by which the lamellar-to-MLV transition under shear flow involves an intermediate identified as multilamellar cylinders, which resembles the myelin figures.[57] Because of this strong parallel, it appears instructive to further consider whether the underlying mechanisms driving the morphological change might also be related. Previous studies describe the formation of the onion phase from their lamellar precursors in terms of a shear-induced elastic buckling instability. Briefly, theory suggests that the shear flow generates an effective force on the lamellar phase, which acts to reduce the membrane area and suppress short-wavelength thermal undulations. Constrained within the lamellar geometry of fixed area, the bilayers under shear thus experience a lateral pressure, which beyond a threshold shear gives rise to a coherent buckling of the lamellae, ultimately leading to the formation of multilamellar vesicles.[58]

Although a detailed comparison is outside the scope of the present enquiry, a phenomenological parallel is in order: The removal of cholesterol necessarily concentrates gel-phase sphingomyelin in the exposed, outermost lamellae of single myelins and decreases the bilayer area.[59] As a consequence, thermal undulation of the lamellae is suppressed, subjecting the residual bilayers to a net mechanical tension and an effective lateral pressure. Under the constraints of fixed macroscopic myelin area, this pressure, beyond a threshold, may orchestrate a coherent buckling of multiple lamellae in a manner similar to that produced by hydrodynamic shear. Indeed, our observations of initial deformations of the myelin boundary producing nascent multilamellar buds (Figure 3B, arrowheads) suggest a cooperative buckling. Because the effective cholesterol concentration in the outer lamellae is probably high, near the solubility limit, it appears reasonable that the elastic buckling can exceed the threshold required to transform the multicylindrical myelins into multilamellar vesicles in a manner akin to shear-induced instabilities in lamellar surfactants.[55]

Second, we investigated binding interactions at the myelin boundaries. For the study, we chose the well-studied case of GM_1-cholera toxin subunit b (CTxB) interaction in which cholera toxin, a member of AB5 family of pentameric proteins, multivalently recognizes up to five copies of a membrane glycolipid, monosialoganglioside GM_1, with an exquisite

https://doi.org/10.1021/acs.langmuir.1c02576
Langmuir 2022, 38, 1045−1056

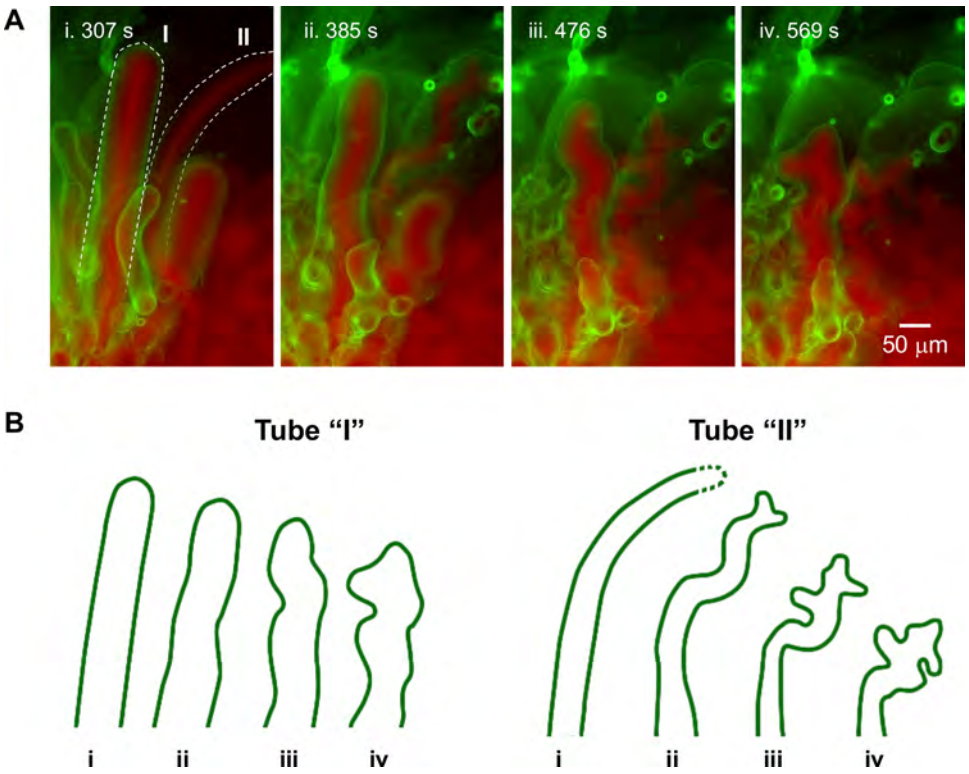

Figure 4. Morphological effect of multivalent ganglioside GM1 and cholera toxin subunit b (CTxB) binding interaction on POPC/SM/Chol/GM_1/Rhod-PE myelin figures. (A) Time-lapse fluorescence micrographs highlight tubular bending to membrane budding transition when myelin figures displaying GM_1 are subjected to CTxB treatment. (B) Schematic of the morphological transition for the myelins marked with dotted lines in (A). Note: the dotted area for Tube "II" is a projection.

biospecificity and strong affinity.[60] We chose this binding pair because previous studies establish that (1) GM_1 partitions within the cholesterol-enriched L_o phase,[42] which in myelin figures preferentially accumulate in the exposed, outer lamellae and (2) the multivalent GM_1-CTxB interactions influence membrane physical properties (e.g., lateral fluidity and local curvatures),[61−64] which within the constraints of myelin geometry might generate unusual response.

In experiments, we added Alexa Fluor 488-conjugated CTxB (AF488-CTxB) to the exterior of the preformed myelin figures, consisting of POPC, sphingomyelin, and cholesterol and labeled with Rhod-PE. Upon addition of AF488-CTxB (0.25−1 mM), we find that the external boundary of the myelin figure becomes uniformly lit with green fluorescence due to AF488-CTxB, consistent with the expected enrichment of its binding partner, GM_1, in the outermost lamellae (Figure 4). Within seconds, these protein-decorated myelins exhibit clear shape changes: The extended fingerlike myelins bend, wrinkle, and bifurcate while retaining their cylindrical motif.

This binding-induced macroscopic shape change in myelin figures suggests another distinct type of elastic instability, which we propose ensues from the unique myelin organization. It is now well established that CTxB, like other related multivalent protein toxins, induces tubular invaginations in single lipid bilayers of giant vesicles and plasma membranes of living cells.[65] These invaginations are known to originate from the synergistic effects of (1) multivalent binding, which allows single CTxB molecules to accumulate up to five GM_1 and (2) higher-density clustering of GM_1-CTxB molecules, which occurs because of the line energy between the more ordered GM_1-CTxB enriched region[61] and the surrounding membrane. These lateral reorganizations locally generate an asymmetric compressive stress, which, in the limit of low to moderate membrane tensions, favor local negative curvatures and provide a driving force for membrane invagination.[65] In myelin figures, these forces compete with the opposing forces unique to myelin molecular organization and geometry. Experimental evidence presented here indicates that the outermost lamellae are enriched in the L_o phase and possess higher lipid order (and thus higher bending rigidity) compared to the inner ones. Because GM_1 preferentially partitions in this phase, the corresponding statistical overabundance of GM_1 facilitates near-complete CTxB coverage. This in turn would further amplify the mismatch in the lipid order in the outermost lamellae (a mere 2 mol % GM_1 is sufficient to decorate the membrane surface with a near-continuous protein layer). As a consequence, the outermost lamellae of CTxB decorated myelins are likely to experience a considerable compressive stress and mechanical tension, which extends over the entire layer (see above). Furthermore, the smectic geometry of the myelin firmly couples the strained outermost lamellae with the inner lamellae along the axial length of the myelin tube and remains fixed over the experimental timescales at the two ends. Taken together, these factors then subject the myelin to a stress differential between the strained outermost bilayer and relaxed lamella in the interior. This scenario has a strong parallel with many different types of layered morphologies in which the differential strain and elasticities of the skin layer (relative to the bulk foundation) generate elastic instabilities that produce bends, loops, and wrinkles.[66−68]

https://doi.org/10.1021/acs.langmuir.1c02576
Langmuir 2022, 38, 1045−1056

CONCLUSIONS

Collectively, the findings presented here exemplify some of the novel emergent characteristics of stress-induced dynamic structures that emerge during nonequilibrium self-organization of lipid amphiphiles in water. They reveal the formation of hierarchically ordered, cylindrical smectic crystals or myelin figures that are compositionally graded displaying extended radial patterns of molecular compositions: cholesterol and saturated sphingomyelin enriching in the outer lamellae and the unsaturated phospholipids concentration in the inner ones. They show that these compositional gradients emerge as a result of the interplay between the kinetic differences in the hydration behaviors of different lipids and the stress-driven myelinic instabilities of insoluble lipids. Furthermore, they show that these initial instabilities couple successively with higher-order elastic instabilities—illustrated for the chemical activities of cholesterol-extracting MβCD and CTxB binding glycolipid GM_1—generating complex morphologies over extended and multiple length scales.

Because compositionally graded myelins exhibit corresponding gradients of elasticity, permeability, and chemical reactivity, our results may pave for myriads of new applications: Can cholesterol-enriched outer lamellae of myelins be used to concentrate and crystallize membrane proteins?[69] Might myelins offer a platform to produce, maintain, and release ionic gradients (store and discharge electrical charges) at the nanometer scale of interlamellar aqueous channels? Can we selectively sequester cargo inside myelin cores? Can we exploit the compositional gradients (and extended multiscale organization) of self-organizing myelins to direct templated synthesis and growth of novel nanostructures in their core and in their interlamellar spacing? Can we put their collective organization into dense labyrinthine packing to use to assemble higher-order patterns? Can we use this as a model system to study tubular and closely juxtaposed intracellular membrane compartments, such as the endoplasmic reticulum and the Golgi apparatus? In the events of lipid extraction from or protein binding on multilamellar membranes, our result may offer insights into possible morphological outcomes. These and other nontraditional applications, we anticipate, will considerably enhance the utility of these fascinating nonequilibrium structures of simple amphiphilic mixtures.

ASSOCIATED CONTENT

Supporting Information

The Supporting Information is available free of charge at https://pubs.acs.org/doi/10.1021/acs.langmuir.1c02576.

Experimental configuration, SAXS measurements of myelins, fluorescence micrographs of POPC/SM/Chol (44.8.45:10) myelin figures, Laurdan generalized polarization (GP) analysis of myelins, FRAP measurements of phase-sensitive probe lipids in myelins, interfacial reorganization in the lipid plague, morphological characterization of the dry lipid state exposed to ambient humidity, and additional fluorescence micrographs of MbCD-treated myelins (PDF)

Typical POPC myelin figure formation (MOV)

Typical POPC/sphingomyelin/cholesterol myelin figure formation (MOV)

Morphological effect of graded extraction of cholesterol by methyl beta-cyclodextrin (MβCD) on POPC/SM/Chol/Rhod-PE/NBD-PE myelin figures (MOV)

Morphological effect of graded extraction of cholesterol by methyl beta-cyclodextrin (MβCD) on POPC/SM/Chol/Rhod-PE/NBD-PE myelin figures (MOV)

Morphological effect of multivalent ganglioside GM1 and cholera toxin subunit b (CTxB) ligand-receptor interaction on POPC/SM/Chol/GM1/Rhod-PE myelin figures (MOV)

AUTHOR INFORMATION

Corresponding Authors

Atul N. Parikh − *Centre for Biomimetic Sensor Science, Nanyang Technological University, 637553, Singapore; School of Materials Science and Engineering, Nanyang Technological University, 639798, Singapore; Departments of Chemistry and Biomedical Engineering, University of California, Davis, California 95616, United States;* orcid.org/0000-0002-5927-4968; Email: anparikh@ucdavis.edu

Bo Liedberg − *Centre for Biomimetic Sensor Science, Nanyang Technological University, 637553, Singapore; School of Materials Science and Engineering, Nanyang Technological University, 639798, Singapore;* orcid.org/0000-0003-2883-6953; Email: bliedberg@ntu.edu.sg

Authors

James C. S. Ho − *Centre for Biomimetic Sensor Science, Nanyang Technological University, 637553, Singapore; School of Materials Science and Engineering, Nanyang Technological University, 639798, Singapore*

Wan-Chih Su − *Departments of Chemistry, University of California, Davis, California 95616, United States*

Xuan Chun Wang − *Centre for Biomimetic Sensor Science, Nanyang Technological University, 637553, Singapore*

Complete contact information is available at: https://pubs.acs.org/10.1021/acs.langmuir.1c02576

Author Contributions

The manuscript was written through contributions of all authors. All authors have given approval to the final version of the manuscript. J.C.S.H., W-C.S., and X.C.W. performed the experiments and analyzed the data. J.C.S.H., W-C.S., X.C.W., A.N.P., and B.L. interpreted the data and wrote the manuscript.

Notes

The authors declare no competing financial interest.

ACKNOWLEDGMENTS

The authors acknowledge the use of EM facilities at the NTU Institute of Structural Biology. J.C.S.H., A.N.P., and B.L. acknowledge support from the Provost Office, the School of Materials Science & Engineering, and the Strategic Initiative on Biomimetic and Sustainable Materials (IBSM), Nanyang Technological University. The authors also acknowledge the support from the Ministry of Education Singapore (grant no. MOE2018-T2-1-025). J.C.S.H. also acknowledges the support from Singapore Centre for Environmental Life Sciences Engineering (SCELSE). W-C.S. and A.N.P. acknowledge support from the National Science Foundation (United States) through a grant from the Division of Materials Research

(#1810540). A.N.P.'s contributions are also supported by a grant from the U.S. National Science Foundation (DMR-2104123).

REFERENCES

(1) Laughlin, R. G. *The Aqueous Phase Behavior of Surfactants*; Academic Press: London San Diego, 1994.
(2) Gelbart, W.; Ben-Shaul, A.; Roux, D. *Micelles, Membranes, Microemulsions, and Monolayers*; Springer-Verlag: New York, 1994.
(3) Fialkowski, M.; Bishop, K. J. M.; Klajn, R.; Smoukov, S. K.; Campbell, C. J.; Grzybowski, B. A. Principles and implementations of dissipative (dynamic) self-assembly. *J. Phys. Chem. B* **2006**, *110*, 2482−2496.
(4) Mann, S. Self-assembly and transformation of hybrid nano-objects and nanostructures under equilibrium and non-equilibrium conditions. *Nat. Mater.* **2009**, *8*, 781−792.
(5) Cross, M. C.; Hohenberg, P. C. Pattern-formation outside of equilibrium. *Rev. Mod. Phys.* **1993**, *65*, 851−1112.
(6) Mattia, E.; Otto, S. Supramolecular systems chemistry. *Nat. Nanotechnol.* **2015**, *10*, 111−119.
(7) Boullerne, A. I. The history of myelin. *Exp. Neurol.* **2016**, *283*, 431−445.
(8) Virchow, R. On the general appearance of the nerve-like structures from animal substances. *Virchows Arch.* **1854**, *6*, 562.
(9) Sakurai, I.; Kawamura, Y. Growth-mechanism of myelin figures of phosphatidylcholine. *Biochim. Biophys. Acta, Biomembr.* **1984**, *777*, 347−351.
(10) Buchanan, M.; Egelhaaf, S. U.; Cates, M. E. Dynamics of interface instabilities in nonionic lamellar phases. *Langmuir* **2000**, *16*, 3718−3726.
(11) Haran, M.; Chowdhury, A.; Manohar, C.; Bellare, J. Myelin growth and coiling. *Colloids Surf., A* **2002**, *205*, 21−30.
(12) Zou, L. N.; Nagel, S. R. Stability and growth of single myelin figures. *Phys. Rev. Lett.* **2006**, *96*, No. 138301.
(13) Zou, L. N. Myelin figures: The buckling and flow of wet soap. *Phys. Rev. E* **2009**, *79*, No. 061502.
(14) Reissig, L.; Fairhurst, D. J.; Leng, J.; Cates, M. E.; Mount, A. R.; Egelhaaf, S. U. Three-Dimensional Structure and Growth of Myelins. *Langmuir* **2010**, *26*, 15192−15199.
(15) Chaieb, S.; Sutin, J. In *Growth of Myelin Figures Made of Water Soluble Surfactant*, 1st Annual International IEEE-EMBS Special Topic Conference on Microtechnologies in Medicine and Biology. Proceedings (Cat. No. 00EX451), IEEE, 2000; pp 345−348.
(16) Dave, H.; Surve, M.; Manohar, C.; Bellare, J. Myelin growth and initial dynamics. *J. Colloid Interface Sci.* **2003**, *264*, 76−81.
(17) Mishima, K.; Yoshiyama, K. Growth rate of myelin figures of egg-yolk phosphatidylcholine. *Biochim. Biophys. Acta, Biomembr.* **1987**, *904*, 149−153.
(18) Sakurai, I.; Suzuki, T.; Sakurai, S. Structure and growth-behavior of myelin figures. *Mol. Cryst. Liq. Cryst.* **1990**, *180*, 305−311.
(19) Taribagil, R.; Arunagirinathan, M. A.; Manohar, C.; Bellare, J. R. Extended time range modeling of myelin growth. *J. Colloid Interface Sci.* **2005**, *289*, 242−248.
(20) Warren, P. B.; Buchanan, M. Kinetics of surfactant dissolution. *Curr. Opin. Colloid Interface Sci.* **2001**, *6*, 287−293.
(21) Huang, J. R.; Cheng, Y. C.; Huang, H. J.; Chiang, H. P. Confocal mapping of myelin figures with micro-Raman spectroscopy. *Appl. Phys. A: Mater. Sci. Process.* **2018**, *124*, No. 58.
(22) Kennedy, A. P.; Sutcliffe, J.; Cheng, J. X. Molecular composition and orientation in myelin figures characterized by coherent anti-stokes Raman scattering microscopy. *Langmuir* **2005**, *21*, 6478−6486.
(23) Sakurai, I.; Suzuki, T.; Sakurai, S. Cross-sectional view of myelin figures. *Biochim. Biophys. Acta, Biomembr.* **1989**, *985*, 101−105.
(24) Stoeckenius, W. An electron microscope study of myelin figures. *J. Biophys. Biochem. Cytol.* **1959**, *5*, 491−500.
(25) Santangelo, C. D.; Pincus, P. Coiling instabilities of multilamellar tubes. *Phys. Rev. E* **2002**, *66*, No. 061501.
(26) Huang, J. R. Theory of myelin coiling. *Eur. Phys. J. E* **2006**, *19*, 399−412.
(27) Mullins, W. W.; Sekerka, R. F. Stability of planar interface during solidification of dilute binary alloy. *J. Appl. Phys.* **1964**, *35*, 444−451.
(28) Helfrich, W. Steric interaction of fluid membranes in multilayer systems. *Z. Naturforsch., A: Phys. Sci.* **1978**, *33*, 305−315.
(29) Conrad, M. Information processing in molecular systems. *Biosystems* **1972**, *5*, 1−14.
(30) Veatch, S. L.; Keller, S. L. Seeing spots: Complex phase behavior in simple membranes. *Biochim. Biophys. Acta, Mol. Cell Res.* **2005**, *1746*, 172−185.
(31) Israelachvili, J. N.; Marcelja, S.; Horn, R. G. Physical principles of membrane organization. *Q. Rev. Biophys.* **1980**, *13*, 121−200.
(32) Shimshick, E. J.; McConnell, H. M. Lateral phase separation in phospholipid membranes. *Biochemistry* **1973**, *12*, 2351−2360.
(33) Evans, E.; Needham, D. Physical properties of surfactant bilayer membranes: thermal transitions, elasticity, rigidity, cohesion and colloidal interactions. *J. Phys. Chem. A* **1987**, *91*, 4219−4228.
(34) Veatch, S. L.; Keller, S. L. Miscibility phase diagrams of giant vesicles containing sphingomyelin. *Phys. Rev. Lett.* **2005**, *94*, No. 148101.
(35) Peddireddy, K.; Kumar, P.; Thutupalli, S.; Herminghaus, S.; Bahr, C. Myelin Structures Formed by Thermotropic Smectic Liquid Crystals. *Langmuir* **2013**, *29*, 15682−15688.
(36) Vanag, V. K.; Epstein, I. R. Pattern formation mechanisms in reaction-diffusion systems. *Int. J. Dev. Biol.* **2009**, *53*, 673−681.
(37) Papahadjopoulos, D.; Vail, W. J.; Jacobson, K.; Poste, G. Cochleate lipid cylinders: formation by fusion of unilamellar lipid vesicles. *Biochim. Biophys. Acta, Biomembr.* **1975**, *394*, 483−491.
(38) Leneveu, D. M.; Rand, R. P.; Parsegian, V. A. Measurement of forces between lecithin bilayers. *Nature* **1976**, *259*, 601−603.
(39) Baumgart, T.; Hess, S. T.; Webb, W. W. Imaging coexisting fluid domains in biomembrane models coupling curvature and line tension. *Nature* **2003**, *425*, 821−824.
(40) Baumgart, T.; Hunt, G.; Farkas, E. R.; Webb, W. W.; Feigenson, G. W. Fluorescence probe partitioning between L-o/L-d phases in lipid membranes. *Biochim. Biophys. Acta, Biomembr.* **2007**, *1768*, 2182−2194.
(41) Crane, J. M.; Tamm, L. K. Role of Cholesterol in the Formation and Nature of Lipid Rafts in Planar and Spherical Model Membranes. *Biophys. J.* **2004**, *86*, 2965−2979.
(42) Dietrich, C.; Bagatolli, L. A.; Volovyk, Z. N.; Thompson, N. L.; Levi, M.; Jacobson, K.; Gratton, E. Lipid rafts reconstituted in model membranes. *Biophys. J.* **2001**, *80*, 1417−1428.
(43) Juhasz, J.; Davis, J. H.; Sharom, F. J. Fluorescent probe partitioning in giant unilamellar vesicles of 'lipid raft' mixtures. *Biochem. J.* **2010**, *430*, 415−423.
(44) Tayebi, L.; Ma, Y. C.; Vashaee, D.; Chen, G.; Sinha, S. K.; Parikh, A. N. Long-range interlayer alignment of intralayer domains in stacked lipid bilayers. *Nat. Mater.* **2012**, *11*, 1074−1080.
(45) Yuan, J.; Kiss, A.; Pramudya, Y. H.; Nguyen, L. T.; Hirst, L. S. Solution synchrotron x-ray diffraction reveals structural details of lipid domains in ternary mixtures. *Phys. Rev. E* **2009**, *79*, No. 031924.
(46) Krasnowska, E. K.; Gratton, E.; Parasassi, T. Prodan as a membrane surface fluorescence probe: partitioning between water and phospholipid phases. *Biophys. J.* **1998**, *74*, 1984−1993.
(47) Deegan, R. D.; Bakajin, O.; Dupont, T. F.; Huber, G.; Nagel, S. R.; Witten, T. A. Capillary flow as the cause of ring stains from dried liquid drops. *Nature* **1997**, *389*, 827−829.
(48) Inglefield, P. T.; Lindblom, K. A.; Gottlieb, A. M. Water binding and mobility in the phosphatidylcholine/cholesterol/water lamellar phase. *Biochim. Biophys. Acta, Biomembr.* **1976**, *419*, 196−205.
(49) Filippov, A.; Oradd, G.; Lindblom, G. Influence of cholesterol and water content on phospholipid lateral diffusion in bilayers. *Langmuir* **2003**, *19*, 6397−6400.

https://doi.org/10.1021/acs.langmuir.1c02576
Langmuir 2022, 38, 1045−1056

(50) Filippov, A.; Oradd, G.; Lindblom, G. Lipid lateral diffusion in ordered and disordered phases in raft mixtures. *Biophys. J.* **2004**, *86*, 891−896.
(51) Huang, J.; Buboltz, J. T.; Feigenson, G. W. Maximum solubility of cholesterol in phosphatidylcholine and phosphatidylethanolamine bilayers. *Biochim. Biophys. Acta, Biomembr.* **1999**, *1417*, 89−100.
(52) Ohtani, Y.; Irie, T.; Uekama, K.; Fukunaga, K.; Pitha, J. Differential-effects of alpha-cyclodextrins, beta-cyclodextrins and gamma-cyclodextrins on human-erythrocytes. *Eur. J. Biochem.* **1989**, *186*, 17−22.
(53) Ohvo, H.; Slotte, J. P. Cyclodextrin-mediated removal of sterols from monolayers: Effects of sterol structure and phospholipids on desorption rate. *Biochemistry* **1996**, *35*, 8018−8024.
(54) Simons, B. D.; Cates, M. E. Vesicles and onion phases in dilute surfactant solutions. *J. Phys. II* **1992**, *2*, 1439−1451.
(55) Diat, O.; Roux, D.; Nallet, F. Effect of shear on a lyotropic lamellar phase. *J. Phys. II* **1993**, *3*, 1427−1452.
(56) Kato, T. Shear-Induced Lamellar/Onion Transition in Surfactant Systems. In *Advances in Biomembranes and Lipid Self-Assembly*; Iglic, A.; Rappolt, M.; GarciaSaez, A. J., Eds.; Elsevier Academic Press Inc: San Diego, 2018; Vol. *27*, pp 187−222.
(57) Zipfel, J.; Nettesheim, F.; Lindner, P.; Le, T. D.; Olsson, U.; Richtering, W. Cylindrical intermediates in a shear-induced lamellar-to-vesicle transition. *Europhys. Lett.* **2001**, *53*, 335−341.
(58) Zilman, A. G.; Granek, R. Undulation instability of lamellar phases under shear: A mechanism for onion formation? *Eur. Phys. J. B* **1999**, *11*, 593−608.
(59) Biswas, A.; Kashyap, P.; Datta, S.; Sengupta, T.; Sinha, B. Cholesterol Depletion by M beta CD Enhances Cell Membrane Tension and Its Variations-Reducing Integrity. *Biophys. J.* **2019**, *116*, 1456−1468.
(60) Holmgren, J.; Lönnroth, I.; Månsson, J.; Svennerholm, L. Interaction of cholera toxin and membrane GM1 ganglioside of small intestine. *Proc. Natl. Acad. Sci. U.S.A.* **1975**, *72*, 2520−2524.
(61) Forstner, M. B.; Yee, C. K.; Parikh, A. N.; Groves, J. T. Lipid lateral mobility and membrane phase structure modulation by protein binding. *J. Am. Chem. Soc.* **2006**, *128*, 15221−15227.
(62) Kabbani, A. M.; Kelly, C. V. Nanoscale Membrane Budding Induced by CTxB and Detected via Polarized Localization Microscopy. *Biophys. J.* **2017**, *113*, 1795−1806.
(63) Klenow, M. B.; Jeppesen, J. C.; Simonsen, A. C. Membrane rolling induced by bacterial toxins. *Soft Matter* **2020**, *16*, 1614−1626.
(64) Pezeshkian, W.; Nabo, L. J.; Ipsen, J. H. Cholera toxin B subunit induces local curvature on lipid bilayers. *Febs Open Bio* **2017**, *7*, 1638−1645.
(65) Römer, W.; Berland, L.; Chambon, V.; Gaus, K.; Windschiegl, B.; Tenza, D.; Aly, M. R. E.; Fraisier, V.; Florent, J. C.; Perrais, D.; Lamaze, C.; Raposo, G.; Steinem, C.; Sens, P.; Bassereau, P.; Johannes, L. Shiga toxin induces tubular membrane invaginations for its uptake into cells. *Nature* **2007**, *450*, 670−675.
(66) Efimenko, K.; Rackaitis, M.; Manias, E.; Vaziri, A.; Mahadevan, L.; Genzer, J. Nested self-similar wrinkling patterns in skins. *Nat. Mater.* **2005**, *4*, 293−297.
(67) Savin, T.; Kurpios, N. A.; Shyer, A. E.; Florescu, P.; Liang, H. Y.; Mahadevan, L.; Tabin, C. J. On the growth and form of the gut. *Nature* **2011**, *476*, 57.
(68) Cerda, E.; Mahadevan, L. Geometry and physics of wrinkling. *Phys. Rev. Lett.* **2003**, *90*, No. 074302.
(69) Johansson, L. C.; Wohri, A. B.; Katona, G.; Engstrom, S.; Neutze, R. Membrane protein crystallization from lipidic phases. *Curr. Opin. Struct. Biol.* **2009**, *19*, 372−378.

Recommended by ACS

Identifying the Onset of Phase Separation in Quaternary Lipid Bilayer Systems from Coarse-Grained Simulations
Shushan He and Lutz Maibaum
MARCH 16, 2018
THE JOURNAL OF PHYSICAL CHEMISTRY B
READ

Computation of a Theoretical Membrane Phase Diagram and the Role of Phase in Lipid-Raft-Mediated Protein Organization
Eshan D. Mitra, James P. Sethna, *et al.*
FEBRUARY 12, 2018
THE JOURNAL OF PHYSICAL CHEMISTRY B
READ

Molecular Dynamics Simulations Reveal Leaflet Coupling in Compositionally Asymmetric Phase-Separated Lipid Membranes
Michael D. Weiner and Gerald W. Feigenson
APRIL 22, 2019
THE JOURNAL OF PHYSICAL CHEMISTRY B
READ

Bilayer Membranes with Frequent Flip-Flops Have Tensionless Leaflets
Markus S. Miettinen and Reinhard Lipowsky
MAY 06, 2019
NANO LETTERS
READ

Get More Suggestions >

https://doi.org/10.1021/acs.langmuir.1c02576
Langmuir 2022, 38, 1045−1056